# Reactive-Atom Scattering from Liquid Crystals at the Liquid-Vacuum interface: $[C_{12}mim][BF_4]$ and 4-cyano-4'-octylbiphenyl (8CB)

*Simon M. Purcell,[†] Maria A. Tesa-Serrate,[†] Brooks C. Marshall,[‡] Duncan W. Bruce,[§] Lucía D'Andrea,[§] Matthew L. Costen,[†] John M. Slattery,[§] Eric J. Smoll, Jr.,[‡] Timothy K. Minton,[‡,*] and Kenneth G. McKendrick[†,*]*

[†]Institute of Chemical Sciences, School of Engineering and Physical Sciences, Heriot-Watt University, Edinburgh, EH14 4AS, United Kingdom.

[‡]Department of Chemistry and Biochemistry, Montana State University, Bozeman, Montana 59717, United States.

[§]Department of Chemistry, University of York, Heslington, York YO10 5DD, United Kingdom.

**Received Date:**

KEYWORDS: Ionic liquid, reactive atom scattering, O-atom, liquid crystal, $[C_{12}mim][BF_4]$, 8CB, vacuum interface.

## Abstract

Two complementary approaches were used to study the liquid-vacuum interface of the liquid-

crystalline ionic liquid 1-dodecyl-3-methlyimidazolium tetrafluoroborate ($[C_{12}mim][BF_4]$) in the smectic A (SmA) and isotropic phases. O-atoms with two distinct incident translational energies were scattered from the surface of $[C_{12}mim][BF_4]$. Angle-dependent time-of-flight distributions and OH yields, respectively, were recorded from high and low-energy O atoms. There were no significant changes in the measurements using either approach, nor the properties derived from them, accompanying the transition from the SmA to the isotropic phase. This indicates that the surface structure of $[C_{12}mim][BF_4]$ remains essentially unchanged across the phase boundary, implying that the bulk order and surface structure are not strongly correlated for this material. This effect is ascribed to the strong propensity for the outer surfaces of ionic liquids to be dominated by alkyl chains, over an underlying layer rich in anions and cation head groups, whether or not the bulk material is a liquid crystal. In a comparative study, the OH yield from the surface of the liquid crystal, 8CB, was found to be affected by the bulk order, showing a surprising step increase at the SmA–nematic transition temperature, whose origin is the subject of speculation.

## Introduction

Liquid-crystalline materials represent a state of matter between the solid and liquid where there is long-range molecular positional and/or orientational order. In the presence of a solid or gas interface, the liquid crystal surface structure is perturbed and the surface orientational and positional order can differ from that in the bulk. While this effect is well understood in neutral liquid crystals,[1] it is not, however, yet understood in ionic liquids (ILs). ILs are composed solely of ions and can also have liquid-crystalline states. The physical properties of ILs are widely tunable by varying the cation or anion, making them of interest for many different surface[2] and

bulk applications.[3] Room-temperature ILs and ionic liquid crystals (ILCs) typically consist of an inorganic anion and a bulky (or anisotropic for ILCs), organic cation. The flexibility, size, and shape of the cation reduces the magnitude of the lattice enthalpy and increases the lattice entropy of the IL (compared to a salt such as NaCl), thus favoring the liquid state and lowering the melting point (<100 °C) such that many ILs are often liquid at room temperature.[4, 5] In neutral, organic liquid crystals, the mesophase is promoted by structural anisotropy expressed typically by an extended molecular core of two or three six-membered rings (usually aromatic or heteroaromatic) with, normally, two terminal alkyl chains, leading to anisotropic dispersion forces that are able to stabilize the anisotropic fluid. ILCs differ slightly in that the presence of the charge means that intermolecular associations are driven to a large degree by electrostatic forces, with anisotropy being provided by extended alkyl chains. To preserve the overall anisotropy needed for a liquid crystal phase to exist, smaller anions and larger cations are favored. Thus, for example, 1-alkyl-3-methylimidazolium ([$C_n$mim][X], where *n* is the number of carbon atoms in the alkyl chain and X is the anion) salts show liquid crystallinity for chains containing twelve and fourteen carbon atoms for smaller anions such as tetrafluoroborate ($BF_4^-$) and hexafluorophosphate ($PF_6^-$), respectively, whereas with the larger bis(trifluoromethylsulfonyl)imide ($Tf_2N^-$) anion, the liquid crystalline phase only occurs for very long alkyl chains (*n*=22).[6, 7]

There have been extensive studies of the surfaces of conventional or non-ionic LCs, driven by industrial LC applications,[8, 9] and it is well known that surface-induced smectic order at the free surface (i.e. gas-liquid or vacuum-liquid interface) of liquid-crystalline materials can occur above the transition temperature.[1] This induced smectic order is homeotropic, where the long molecular axis is, on average, oriented parallel to the surface normal. Termed pre-transitional

layering, the number of smectic layers, and their correlation depend strongly on temperature and can occur in the nematic[10, 11] (N) and isotropic (Iso) phases.[12, 13] As the bulk temperature is lowered and a smectic A (SmA) phase is approached, the number of smectic layers at the surface increases, penetrating further into the bulk. Eventually, at the bulk SmA transition temperature, the number of layers diverges and the bulk material adopts the long-range order of the SmA phase.

The surface behavior of ionic liquids is less well understood because of the complex interplay between the Coulombic, van der Waals, and dipolar forces. This is evident in the bulk isotropic phase for ionic liquids both with and without mesophases. Studies have shown that three different types of ordering can occur in the bulk, namely short-distance cation-anion; nearest neighbor cation-cation or anion-anion interactions; and longer-distance alkyl chain aggregations (local lamellar periodicity).[14, 15, 16, 17] A result of these interactions is that at the ionic liquid surface, for materials which show no liquid-crystalline behavior, experiment[18, 19, 20] and simulation[21, 22, 23] have shown a surface-induced layering, whereby the polar head group is oriented toward the bulk and the alkyl chains protrude from the surface. Underneath this alkyl-rich layer, a polar region exists where the charged head groups and anions predominate. The thickness and roughness of the layers present at the free surface depend strongly on the ionic liquid and its environment. Additionally, the number of layers is not sharply defined: periodic density oscillations of the different constituents occur, which are generally damped and tend toward the bulk average as a function of distance from the surface. Understanding the free-surface structure of ionic and non-ionic liquid crystals offers the opportunity of optimizing the free surface for specific applications.[24] Also, specific to liquid-crystalline ILs, the enhanced spatial and orientational order of a mesophase can help in the orientation and immobilization of a

catalyst in thin ionic liquid films on porous substrates.[25] Therefore, for surface-specific applications of ionic liquids, it is important to understand how the surface structure may be influenced by changes in the bulk order.

Although the correlation between bulk and surface order has been well characterized in neutral LCs, there have been relatively few studies that compare the free surface of an ILC between mesophases. An X-ray reflectometry study[26] of the surface of $[C_{18}mim][PF_6]$ using ~150 Å films on a Si substrate found that the layer spacing increased in the SmA phase compared to the crystal structure. This was attributed to the cations rotating to orient their alkyl chains closer to the surface normal, increasing the thickness of each smectic layer. No such layering was found in the isotropic phase. The authors made note, however, that their system may not have been sensitive to surface-induced structure at the interfacial regions. A more recent study[27] using He atom scattering found that for a thin film (8 layers ~36 Å) of $[C_2mim][Tf_2N]$, which does not have a liquid crystal phase, deposited on Au, there was no abrupt change in the scattered He signal, indicating no significant change in surface structure between the solid and liquid phases. Although it is obvious that the liquid-crystalline phase of an ionic liquid affects the bulk properties, the extent to which the bulk order can affect the free surface is currently unknown.

In this paper, efforts to understand this effect are reported. Reactive O-atom scattering has been used to study the free surface of the ionic liquid crystal 1-dodecyl-3-methylimidazolium tetrafluoroborate ($[C_{12}mim][BF_4]$), which has a SmA phase occurring near room temperature, in °C,[28]

Cr • 26.4 • SmA • 38.5 • Iso.

The ionic liquid results are compared against those for the well-known liquid crystal, 4-cyano-4'-octylbiphenyl (8CB), which exhibits SmA and N phases with the following transition temperatures, in °C,[29]

Cr • 21.5 • SmA • 33.5 • N • 40.5 • Iso.

The surface behavior of 8CB has been well-studied experimentally[11, 29, 30] and has been investigated more recently using atomistic simulations with validated force fields.[31] The picture obtained from these different approaches is remarkably consistent, providing a good understanding of free-surface behavior.

The experimental techniques used to probe the ionic liquid surface can be broadly separated into methods that are sensitive to density and orientational order in the layers induced by the surface (e.g., X-ray[18, 26, 32] and neutron reflectometry,[19] ellipsometry[33, 34]) and methods that can probe the chemical composition or molecular orientation of the extreme outer layer (e.g., low-energy ion scattering,[35, 36, 37], X-ray photoelectron spectroscopy,[38, 39, 40, 41] sum frequency generation,[42, 43] and inelastic atomic[27, 44] and molecular[22, 45] scattering). Reactive-atom scattering provides information on the surface composition and on the scattering dynamics of the products formed. Building upon previous work on inelastic atom scattering from solids[46] and PFPE liquid surfaces[47] and on reactive scattering from saturated hydrocarbon surfaces,[48, 49, 50] O-atom reactive scattering can now be interpreted reliably to provide a detailed understanding of the ionic liquid surface.[51]

O-atoms are useful as a surface probe because they can react with hydrocarbon groups at the liquid surface to form OH or $H_2O$ and, since not all of the O-atoms react, insight can be gained by also detecting the inelastically scattered O-atoms. In this paper, two complementary approaches have been used to probe the ionic liquid crystal surface. In the first approach, O($^3P$)

atoms were created by laser photolysis of a gas-phase precursor, $NO_2$, and the nascent OH was detected using laser-induced fluorescence. This method is termed RAS-LIF, meaning reactive-atom scattering with detection *via* laser-induced fluorescence. The second approach used a laser detonation source to form a beam of $O(^3P)$ atoms. The inelastically scattered O-atoms and nascent products, OH and $H_2O$, were detected *via* quadrupole mass spectrometry. This method is termed RAS-MS.

Aside from the detection method, RAS-LIF and RAS-MS differ in the translational energy of the incident O-atoms. RAS-LIF has a much lower average translational energy compared to RAS-MS and, as discussed later, RAS-LIF is consequently strongly and specifically sensitive to the presence of $CH_2$ groups in the alkyl chain.[51] RAS-LIF measurements are always normalized against a reference liquid to remove systematic experimental variations and, as in previous studies,[51] the saturated hydrocarbon, squalane (2,6,10,15,19,23-hexamethyltetracosane), was used. For higher-temperature measurements, $[C_{12}mim][Tf_2N]$, for which previous temperature dependent RAS-LIF measurements have been performed,[52] was used as the reference liquid. In this way, RAS-LIF serves as a precise indicator of the relative density of secondary hydrocarbon groups at the ionic liquid surface.

In RAS-MS, typical incident $O(^3P)$ translational energies are such that all hydrocarbon groups are amenable to hydrogen abstraction.[50, 53, 54] RAS-MS can detect the O, OH, and $H_2O$ scattered fluxes as a function of their arrival time and, in the way the experiment is configured, can also determine the angular distributions of the scattered products, yielding information about surface roughness. By measuring the translational energy of the nascent species, the fraction of the incident kinetic energy that is retained can be deduced, giving information about the number of

surface atoms that are involved in the gas-liquid collision. This can be interpreted in terms of surface hardness or softness in comparison to other liquids.[55]

## Experimental Methods

### Materials

The molecular structures of the materials used in this study are shown in Figure 1. The ionic liquid $[C_{12}mim][BF_4]$ used in the RAS-LIF and RAS-MS experiments was supplied by IoLiTec (Germany); the stated purity was >98%, halide content <100 ppm, and water content <0.1%. 4-Cyano-4'-octylbiphenyl, or 8CB, was purchased from Synthon (Germany) and had a purity of >99.5%. In the RAS-LIF experiments, two reference liquids were used: the branched hydrocarbon squalane (99%), supplied by Sigma Aldrich, and $[C_{12}mim][Tf_2N]$, prepared as part of this study. The synthesis of $[C_{12}mim][Tf_2N]$ is described in the Supporting Information (SI) along with the corresponding NMR data. In all of the experiments, $[C_{12}mim][BF_4]$, 8CB, and the reference liquids were left overnight to degas under high vacuum ($<10^{-6}$ mbar). The vapor pressure of ILs is generally negligible,[56] while the vapor pressure of 8CB is $<10^{-5}$ mbar[57] at room temperature, which made both materials suitable for study in vacuum.

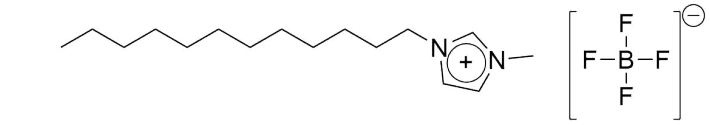

$[C_{12}mim][BF_4]$

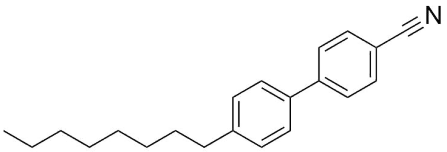

4-cyano-4'-octylbiphenyl (8CB)

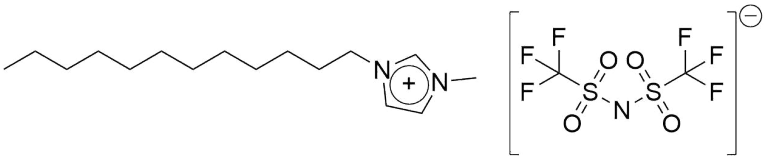

$[C_{12}mim][Tf_2N]$

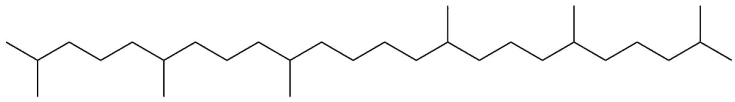

Squalane

**Figure 1.** Chemical structures of materials used.

**RAS-LIF**

A schematic diagram of the key components of the RAS-LIF apparatus is shown in Figure 2a. A brief experimental description is given here and more information is presented in the SI. The experiments were conducted inside a vacuum chamber that contained a rotatable carousel. This allowed multiple liquids to be studied in succession without breaking the vacuum. The carousel consisted of four 5 cm diameter wheels, each partially immersed in a stainless steel bath containing 4-5 mL of liquid. The wheels rotated at 30 rpm, which dragged a film of liquid onto

the wheel to provide a refreshed liquid surface; a standard technique for creating liquid surfaces in vacuum.[58] To present each liquid surface for study, the carousel was rotated about the center axle in increments of 90°. To help create a uniform film of $[C_{12}mim][BF_4]$ or 8CB on the wheel surface, a scraper positioned approximately 0.5 mm from the wheel surface was used. This was particularly important when the materials were in their liquid-crystalline states.

The O($^3P$) atoms were created by photolysis of $NO_2$ (98%, BOC) at a pressure of $1.3 \times 10^{-3}$ mbar using 60 mJ of 355 nm radiation from a frequency-tripled Nd:YAG laser, which passed parallel to the liquid surface. The corresponding average laboratory frame O($^3P$) translational energy was 15.8 kJ mol$^{-1}$, with a FWHM of 26 kJ mol$^{-1}$.[59] The incident O($^3P$) atoms reacted at the liquid-vacuum interface to form OH radicals that were detected by exciting on the $A^2\sum \leftarrow X^2\prod(1,0)$ band and collecting the resulting fluorescence on the $A^2\sum \rightarrow X^2\prod(1,1)$ band. Excitation was achieved *via* a probe beam which counter-propagated with respect to the photolysis beam. The probe beam was wavelength tunable between 281 and 283 nm, with an energy of 250 μJ per pulse, and was produced by the frequency-doubled output of a dye laser. The OH fluorescence was collected using a liquid light guide placed perpendicular to the laser beam axis. Dichroic filters were used to isolate the fluorescence before being detected by a photomultiplier tube.

Temperature control of the liquids was provided by an external oil circulator which flowed oil through channels in the carousel. The temperature of $[C_{12}mim][BF_4]$ or 8CB was inferred by a submersed thermocouple in the squalane reference liquid bath, providing temperature measurements with a precision of ±0.5 ºC; the systematic uncertainty was estimated to be within ±2.0 ºC.

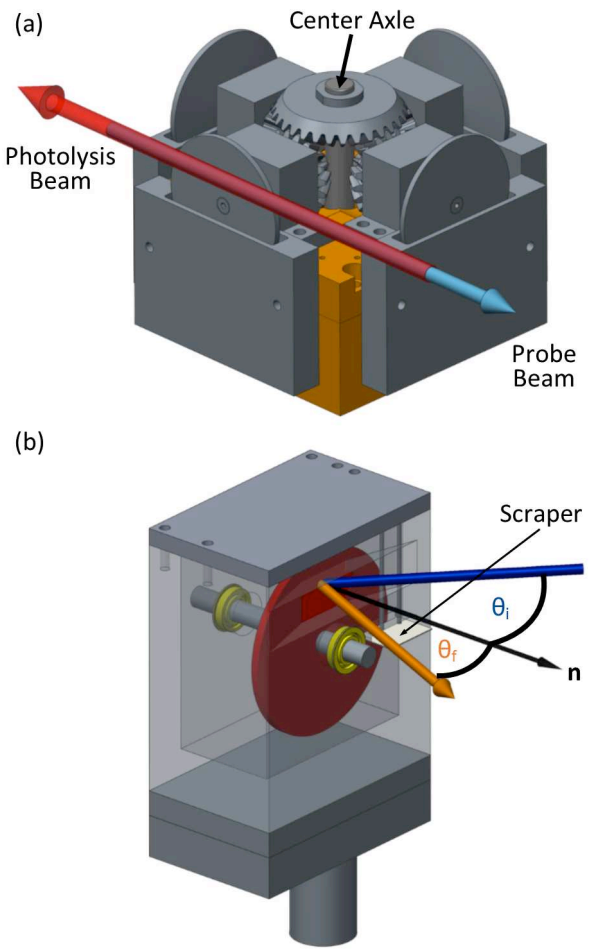


**Figure 2:** a) Schematic diagram of carousel comprising four liquid reservoirs, which was used for RAS-LIF studies. b) Schematic diagram of the liquid reservoir for RAS-MS studies, showing how the incidence angle, $\theta_i$ (blue), final angle, $\theta_f$, (orange), and surface normal, **n**, (black) are defined.

The RAS-LIF experiment was operated in two modes: either the LIF signal from nascent OH molecules was recorded as a function of delay between the photolysis and probe pulses, termed an appearance profile, or the delay was fixed and the probe wavelength was varied to record rotationally resolved OH LIF excitation spectra. To measure appearance profiles at a particular liquid temperature, the laser wavelength was fixed on the most intense line ($Q_1(1)$) and the carousel was rotated such that the liquid bath of interest was in the active position, with its liquid

covered wheel surface presented to the probe and photolysis beams. After recording the OH fluorescence at each delay between the photolysis and probe lasers, the bath containing the reference liquid was then rotated into the active position and the measurement repeated. The nascent OH LIF signal from the liquid of interest was normalized to that from the reference liquid. This process removed systematic variations in the experiment. It is noted that the $Q_1(1)$ line has an overlapping $R_2(3)$ line originating from the upper spin orbit state, which contributes slightly to the OH LIF signal. This overlapping line could not be resolved by the probe laser.

In this study, only two adjacent baths were used: one contained the reference liquid ($[C_{12}mim][Tf_2N]$ or squalane) and the other contained either 8CB or $[C_{12}mim][BF_4]$. For 8CB, only squalane was used as a reference liquid and studies were limited to an upper temperature of 50 °C because the 8CB vapor pressure became problematic at higher temperatures. $[C_{12}mim][BF_4]$ was studied using $[C_{12}mim][Tf_2N]$ and squalane as reference liquids. When squalane was used, the experiment was conducted at liquid temperatures of 30.5 °C and 65.0 °C with the upper temperature being limited by the squalane vapor pressure. To access higher liquid temperatures of $[C_{12}mim][BF_4]$, $[C_{12}mim][Tf_2N]$, which is isotropic across the temperature range, was used as the reference liquid. The maximum liquid temperature used for $[C_{12}mim][BF_4]$ was 109 °C. The temperature dependence of the OH yield from each reference liquid has been characterized previously.[52, 60] In both cases, a marginal increase in OH yield (<10%) is expected across the temperature range studied.

The activation energy for an $O(^3P)$ atom to abstract a secondary hydrogen from an alkyl chain is ~19 kJ $mol^{-1}$,[53] whereas H abstraction by $O(^3P)$ from the methyl groups is larger at ~29 kJ $mol^{-1}$. The head group hydrogens (ring hydrogens plus methyl group at position 3 on the ring) are also expected not to react based on previous measurements of $[C_2mim][Tf_2N]$ in a separate study.[52]

Given the incident average energy of the O($^3P$) atoms, this means RAS-LIF is sensitive only to the presence of $CH_2$ units on the alkyl chain on the [$C_{12}$mim] cation. The activation energies for H abstraction from the phenyl groups of 8CB have not been measured or calculated. However, based on the gas-phase reaction, $O(^3P) + C_6H_6 \rightarrow C_6H_5 + OH$, which is endothermic by 32 kJ mol$^{-1}$,[61] we expect the phenyl-group contribution to the OH signal to be negligible.

**RAS-MS**

The RAS-MS experiments were conducted using a crossed-beams apparatus modified for surface scattering and a hyperthermal oxygen beam which have both been described in detail elsewhere.[50, 51, 62] Additional information pertinent to this study is given in the SI. In brief, the oxygen beam consisted of ground-state atomic oxygen, O($^3P$),[63] and molecular oxygen, $O_2$ ($^3\Sigma_g^-$),[54] and had an average mole fraction of oxygen atoms of 86% with the balance being molecular oxygen. The beam was velocity-selected using a chopper wheel and had an average incident energy of 532 kJ mol$^{-1}$ (FWHM 93 kJ mol$^{-1}$). It was directed onto the liquid surface at a fixed angle of incidence, $\theta_i$ = 60°, with respect to the liquid surface normal. The scattered products were detected by a mass spectrometer which rotated in a plane perpendicular to the liquid surface, to define a final angle, $\theta_f$. Figure 2b shows the liquid reservoir with the angle of incidence of the O-atom beam, $\theta_i$, and final angle, $\theta_f$, defined with respect to the surface normal, **n**. The reservoir was filled with [$C_{12}$mim][$BF_4$] (~25 mL) and a stainless steel wheel (diameter 5 cm) was partially immersed in the liquid. The wheel rotated at 15 rpm to provide a continuously refreshed surface. A sapphire scraper was used to create a film approximately 100 $\mu$m thick on the wheel. For the temperatures used, a visual inspection confirmed that the wheel was well

wetted by the SmA and isotropic phases of $[C_{12}mim][BF_4]$. The reservoir was temperature controlled with an estimated uncertainty in the liquid temperature of ±1 ºC.

After striking the liquid surface, the inelastically scattered O-atoms and reactively scattered products flew into a triply differentially pumped vacuum chamber that housed the detector, where the scattered products were ionized by an electron bombardment ionizer.[64] The resulting ions were then filtered by a quadrupole mass analyzer and detected by a Daly-type ion counter[65] to create a time-of-flight (TOF) distribution. TOF distributions were collected for mass-to-charge ratios of $m/z$ = 16, 17, 18, and 32, which corresponded to $O^+$, $OH^+$, $H_2O^+$, and $O_2^+$, respectively. $O_2$ and $H_2O$ can dissociate during ionization which adds a systematic signal to the O and OH TOFs, respectively. This was corrected by subtracting a fraction of the $O^+$ and $OH^+$ signals corresponding to dissociative ionization of $O_2$ and $H_2O$, respectively, from the total accumulated TOF distributions at $m/z$ = 16 and 17. The magnitude of the fraction was determined by measuring the cracking patterns of $O_2$ and $H_2O$. TOFs were collected over the angular range $-10° \leq \theta_f \leq 75°$, which was limited by the geometry of the liquid reservoir and the scattering chamber.

## Results

### RAS-LIF $[C_{12}mim][BF_4]$

Figure 3a shows OH appearance profiles for $[C_{12}mim][BF_4]$ at liquid temperatures of 30.5 ºC and 65.0 ºC, corresponding to the SmA and Iso phases of $[C_{12}mim][BF_4]$, respectively. Both appearance profiles have been normalized to the maximum OH LIF signal from the reference liquid, $[C_{12}mim][Tf_2N]$, which was recorded at the same temperature and immediately after the $[C_{12}mim][BF_4]$ measurement. Also shown in Figure 3a is a self-normalized $[C_{12}mim][Tf_2N]$ appearance profile at 65.0 ºC. The corresponding appearance profile for $[C_{12}mim][Tf_2N]$ at 30.5

ºC was nearly identical, consistent with the known minimal temperature dependence for this liquid. Nine appearance profiles were recorded at each temperature to create an average with the associated error bars representing 95% confidence limits (CL). All of the appearance profiles for $[C_{12}mim][BF_4]$ and $[C_{12}mim][Tf_2N]$ were corrected for a small, systematic (~2%) contribution from inelastically scattered OH, formed by dissociation of a HONO impurity by the photolysis laser. HONO was formed in the chamber due to the reaction between the $NO_2$ precursor gas and residual water. The procedure for this correction is described in a previous publication.[51]

LIF is a density detector, which means there is a bias in the experiment towards slower moving OH radicals, which increase the OH density in the probe volume, leading to an increased fluorescence signal. As performed in previous studies,[51] this would nominally necessitate, *via* a numerical simulation, the calculation of compensating density-flux correction factors. However, in Figure 3a it can be seen that the peaks of the appearance profiles from the liquids being compared arrive at the same time (~16 $\mu$s), regardless of temperature. This means there is no significant change in the average OH velocity and hence the appearance profiles can be reliably compared without taking into account the velocity-dependent experimental bias in the system.

Excitation spectra on the $Q_1(N)$ branch of OH from $[C_{12}mim][BF_4]$ were recorded at the peak of the appearance profile (15 $\mu$s) for liquid temperatures of 30.5 °C and 65.0 °C. The probe laser energy was kept constant within ±10%. The spectrum simulation program LIFBASE[66] was then used to extract the rotational populations up to $N = 5$, where $N$ is the rotational quantum number excluding spin. No statistically significant differences between the rotational populations at liquid temperatures of 30.5 °C and 65.0 °C (Figure S3) were found. The derived fractional populations of the $N = 1$ levels were found to be 0.37±0.02 and 0.34±0.03 for 30.5 °C and 65.0 °C, respectively. The quoted errors are 95% CL for five spectra at each liquid temperature. The

goal of the rotational analysis was not to determine absolute rotational populations but to establish whether there were any relative changes between different liquid temperatures. Therefore, no stringent tests were performed to test if the spectra were saturated. As there was no discernible population difference in the $N = 1$ level between liquid temperatures, a universal assumption in the subsequent analysis is that changes in signal recorded on the $Q_1(1)$ and overlapping $R_2(3)$ line are correlated directly with changes in overall OH yield and are not attributed to changes in rotational temperature.

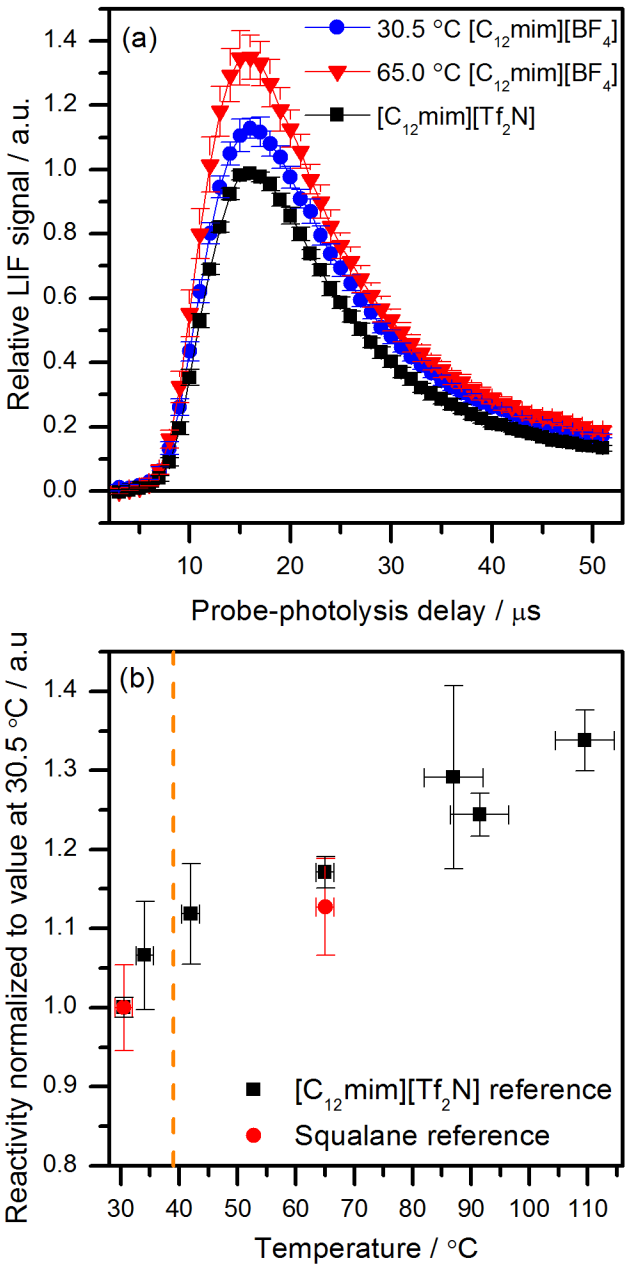


**Figure 3:** a) Appearance profiles for $[C_{12}mim][BF_4]$ normalized to the peak OH LIF signal from $[C_{12}mim][Tf_2N]$ for liquid temperatures of 30.5 °C and 65.0 °C. Reference $[C_{12}mim][Tf_2N]$ profiles were recorded at both temperatures and had nearly identical shapes. For clarity, only the appearance profile from $[C_{12}mim][Tf_2N]$ at a liquid temperature of 65.0 °C is shown. b) $[C_{12}mim][BF_4]$ reactivities normalized to the reactivity at 30.5 °C, referenced to either $[C_{12}mim][Tf_2N]$ or squalane, as shown. *y*-axis error bars represent 95% CL. *x* errors are estimates

and not derived statistically (see text). The SmA–Iso transition temperature is also shown (dashed line).

Having established the absence of any systematic influence of the OH rotational temperature, the nascent OH LIF signal from $[C_{12}mim][BF_4]$ was examined further by recording appearance profiles at additional liquid temperatures. Two or three appearance profiles were recorded for each liquid temperature using $[C_{12}mim][Tf_2N]$ as the reference liquid. The appearance profiles were then integrated between 2 $\mu$s and 30 $\mu$s to give a value here termed *reactivity*. The results are shown (black symbols) in Figure 3b, where the reactivity of $[C_{12}mim][BF_4]$ has been plotted as function of liquid temperature. Each reactivity has been normalized to the reactivity at 30.5 °C; the *y*-axis error bars are 95% CL. With the exception of 30.5 °C and 65.0 °C, which also have 95% CL *x* errors, the *x*-axis error bars were not derived statistically, rather their values are estimates based on the correlation between the circulator temperature and the liquid temperature in the reference bath, since for these particular measurements a thermocouple was not used to monitor the liquid bath temperature.

Figure 3b shows there is a clear linear trend in reactivity in going from 30.5 °C to 109 °C. The reactivity increased by approximately 35% over the ~80 °C temperature range. Also obvious is that there is no discontinuity between the SmA and isotropic phase (dashed line in Figure 3b). Artificial changes in reactivity caused by changes in the nascent OH LIF signal from the $[C_{12}mim][Tf_2N]$ surface as a function of temperature were ruled out by also using squalane as a reference liquid: nine appearance profiles were recorded at 30.5 °C and 65 °C. These results, also plotted (red symbols) in Figure 3b, have been normalized to the reactivity at 30.5 °C. They confirm the linear trend observed using $[C_{12}mim][Tf_2N]$ as the reference liquid.

**8CB**

Figure 4a shows representative appearance profiles recorded from 8CB referenced against squalane at squalane liquid temperatures of 20.0 °C, 25.0 °C, 35.0 °C, and 42.5 °C. While in principle this could correspond to an investigation of the Cr, SmA, N, and Iso phases, respectively, 8CB will be in its SmA phase at 20 °C because 8CB supercools readily and, while formally in a metastable state, it is rather resistant to crystallization. Indeed, the temperature of 20.0 °C was achieved by cooling from room temperature where 8CB is in its SmA phase (assuming that room temperature is > 21.5 °C, which is reasonable). Typically between three and seven appearance profiles were recorded at each temperature. It was found that some fluorescence was excited directly from the 8CB samples by the probe beam. This created an artificial background in the signal gate that was independent of the delay between the photolysis and probe pulses, increasing the level of noise in the 8CB appearance profiles compared to those from $[C_{12}mim][BF_4]$. This meant that making a delay-dependent correction for inelastically scattered OH due to the presence of background HONO, as described above, was not feasible.[51] However, it was still possible to estimate the average contribution to each profile (see SI). A ~1% contribution was estimated to be present in the 8CB and squalane appearance profiles. Since in general the errors are larger than this, any effect can be ignored. Regardless of these minor effects, Figure 4a shows clearly that there are much higher OH signals for the 35.0 °C and 42.5 °C data, corresponding to the nematic and isotropic phases, over those for the 20.0 °C and 25.0 °C (SmA) data.

Excitation spectra were recorded for 8CB at the peak of the appearance profile (15 $\mu$s) on the $R_1(N)$ branch at 20.0 °C, 26.5 °C, 37.0 °C, and 42.5 °C. Typically ten scans were recorded for each temperature. For levels up to $N = 6$, no significant differences were found in the relative

rotational populations between the liquid temperatures (Figure S4). Table 1 shows the fractional populations of the $N = 1$ level and its associated 95% CL.

**Table 1**. Fractional populations for 8CB in OH $N = 1$ and corresponding 95% CL.

| **Temperature / °C** | **Fractional Population** |
|---|---|
| 20.0 | 0.40±0.05 |
| 26.5 | 0.39±0.01 |
| 37.0 | 0.40±0.04 |
| 42.5 | 0.42±0.04 |

Similar to $[C_{12}mim][BF_4]$, this means OH LIF signal changes in the appearance profiles can be attributed directly to changes in reactivity and hence imply changes in either surface structure or composition.

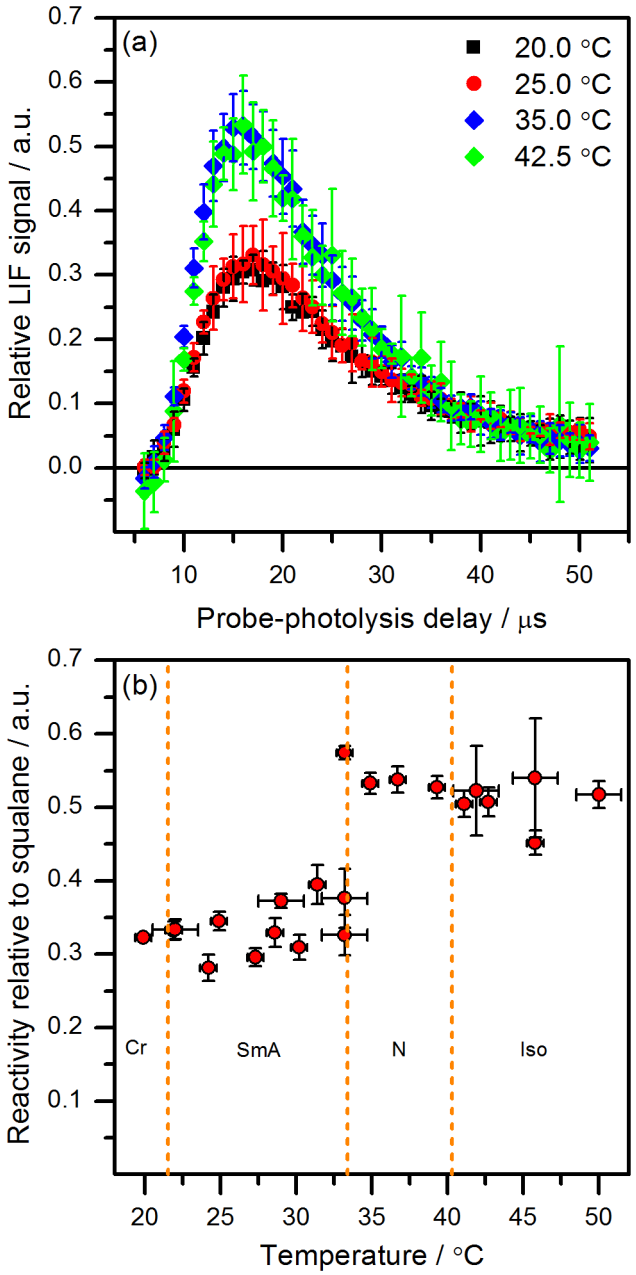


**Figure 4**: a) Representative OH appearance profiles for 8CB at different liquid temperatures normalized to the peak OH LIF signal from squalane. b) Reactivity for 8CB as a function of liquid temperature. Dashed vertical lines indicate bulk transition temperatures. *y* error bars correspond to 95% CL. The smaller *x* error bars correspond to ±0.5 ºC 95% CL, while larger *x* error bars correspond to ±2 ºC, which are estimates of precision in temperature and not derived statistically.

Figure 4b shows the reactivities for 8CB across the full temperature range; these reactivities were calculated by integrating the 8CB appearance profiles between 9 $\mu$s and 30 $\mu$s. They were then normalized to the squalane reactivity averaged over all temperatures. Consistent with Figure 4a, a clear jump in the reactivity occurs at the SmA-to-N transition temperature. On either side of this transition temperature, the reactivity is relatively constant. Therefore, the average increase in reactivity can be found by averaging the reactivities above and below the SmA-N transition temperature. The calculated increase in reactivity was 58±2% with the error being 95% CL.

**RAS-MS [$C_{12}$mim][$BF_4$]**

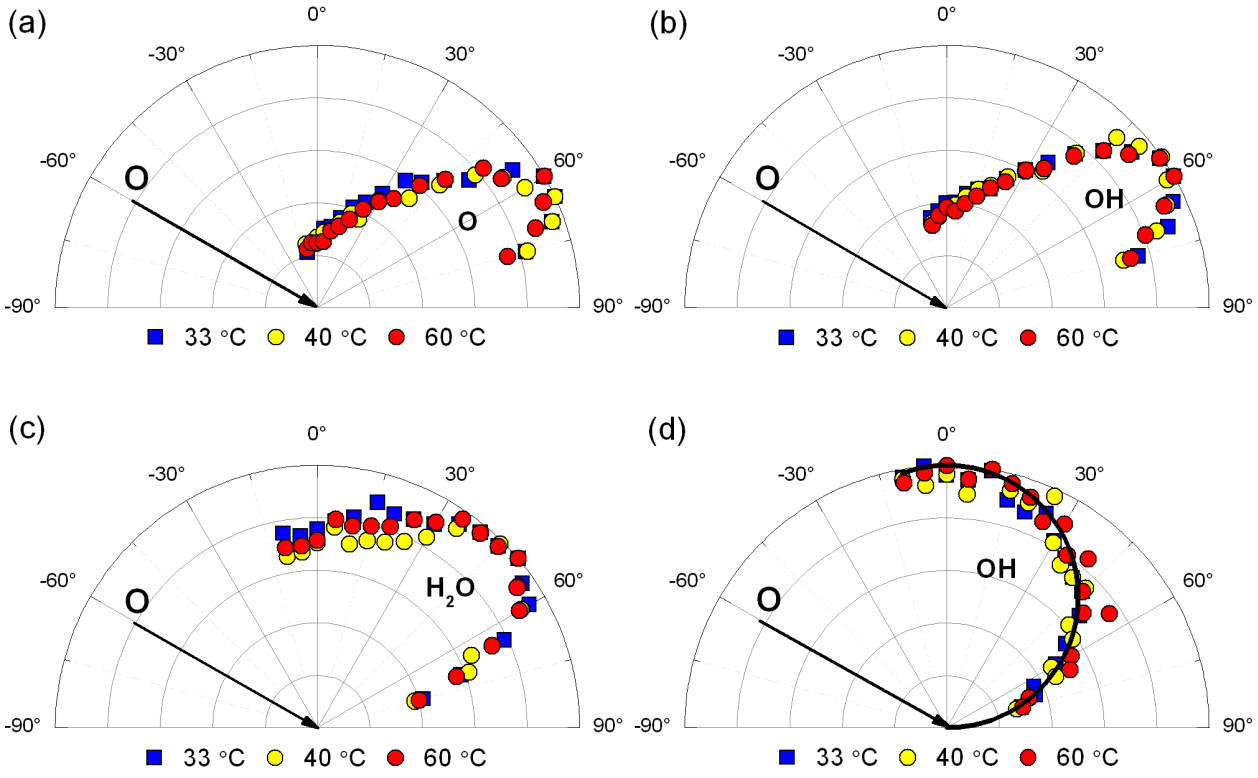

**Figure 5.** a) to c) Normalized IS flux plotted as a function of $\theta_f$ for O, OH, and $H_2O$ with $T$ = 33 °C, 40 °C, and 60 °C. d) OH TD flux as a function of $\theta_f$ for 33 °C, 40 °C, and 60 °C. An ideal TD angular distribution with the form $\cos\theta_f$ is also shown (black line).

Time-of-flight distributions were recorded for the scattered species O, OH, and $H_2O$. These distributions were bimodal and were empirically separated into impulsively scattered (IS) species (arising from an Eley-Rideal type interaction) and thermally desorbed (TD) species (arising from a Langmuir-Hinshelwood type interaction), as done previously in the literature.[54, 67, 68] Further information about the analysis is given in the SI. Here, only IS species are considered as these are interpreted unambiguously as being predominantly from single or few-collision scattering events and are more easily related to surface structure compared to TD species. The respective IS distribution for each $\theta_f$ was integrated to give a flux, proportional to the number of products reaching the detector in a given time interval, or the TOF distributions were used to extract average translational energies of scattered products.[68]

Figures 5a-c show the normalized IS flux for O, OH, and $H_2O$, as $\theta_f$ was varied, collected from the $[C_{12}mim][BF_4]$ surface at temperatures of $T$ = 33 °C, (at which $[C_{12}mim][BF_4]$ is in the smectic A phase) 40 °C, and 60 °C (where both temperatures correspond to the isotropic phase of $[C_{12}mim][BF_4]$). The distributions were normalized to their maximum values, as the beam source conditions were not sufficiently constant to reliably compare the absolute scattered flux between temperatures. The O and OH angular distributions have maxima close to the specular angle ($\theta_f$ = 60°), consistent with previous studies.[50, 54, 55, 68] Of particular note is that there is virtually no difference in the angular distributions for each temperature studied. The angular distribution for $H_2O$, which is much broader compared to O and OH, has a maximum closer to the surface normal and is indicative of a process involving a higher proportion of secondary collisions. This

is expected since the formation of $H_2O$ requires a complex gas-surface interaction and is therefore more likely to scatter in a non-specular way. The dynamics of water formation from $[C_{12}mim][BF_4]$ are discussed briefly in a previous publication.[68] Again, regarding the $H_2O$ product, it is noted that changing the liquid temperature has no distinguishable effect. Figure 5d shows the normalized TD fluxes for OH at 33 °C, 40 °C, and 60 °C. The good agreement between the fitted TD flux for each surface temperature and the $\cos\theta_f$ function, which is expected for thermal desorption, validates the separation of the scattered species into IS and TD components. The lack of temperature dependence of the flux of the scattered species is emphasized further by examining the O/OH and O/$H_2O$ product ratios and also the IS/TD ratios (Figures S6 and S7) as a function of $\theta_f$.

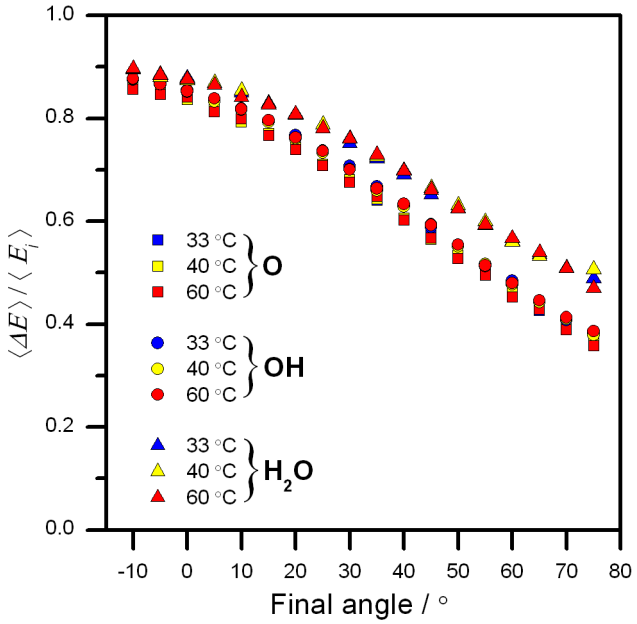


**Figure 6**: Fractional energy loss at the liquid surface for the IS component of scattered O, OH, and $H_2O$ with $T$ = 33 °C, 40 °C, and 60 °C.

Figure 6 shows the average energy loss to the surface, $\langle \Delta E \rangle$, as a proportion of the average incident beam energy, $\langle E_i \rangle$, for O, OH, and $H_2O$ with $T$ = 33 °C, 40 °C, and 60 °C. When $\theta_f$ is

close to 0°, this corresponds to particles leaving the surface that have undergone a relatively low-impact parameter collision that is backscattered in the local center-of-mass frame, consistent with the transfer of more energy[68]. As $\theta_f$ tends toward 60°, the O-atom collisions become more grazing with the surface and less energy is transferred. As noted previously for ionic liquids,[54] impulsively scattered O-atoms transfer the least amount of energy to the surface, followed closely by reactive collisions forming OH and then, with a larger difference, by those producing $H_2O$. These trends can be explained as follows: O-atoms sample all of the surface and can strike the stiffer anion, the head group of the cation or an alkyl chain, all of which have been shown to be present in different proportions at the $[C_{12}mim][BF_4]$ surface.[51] H abstraction to form OH from the $CH_2$ and $CH_3$ groups on the surface is modestly exothermic,[50] but this is negligible relative to the much larger incident O-atom energy, so the OH energy transfer data can in general be readily compared to the O atom results in terms of their respective collision dynamics. For the IS OH to be produced, an O atom must necessarily strike a hydrogen atom. The surrounding atoms in the alkyl chain also take part in the collision, increasing energy transfer through vibrational excitation.[55] This is also true for O atoms that scatter impulsively from alkyl chains, but less so from the stiffer anions or possibly cation head group, resulting in a lower average energy transfer to the surface. IS $H_2O$ results in significantly more energy transferred to the surface, as at least two collisions must be involved, leading to multiple pathways for the formation of IS $H_2O$ (the discussion of which is beyond the scope of this paper). The main feature of interest here is that the temperatures of 33 °C, 40 °C, and 60 °C have no effect on the surface energy transfer, implying once again that the environment experienced by the projectile in both impulsive O-atom and reactive collisions is independent of the bulk order.

## Discussion

**Relation between bulk and surface structure of $[C_{12}mim][BF_4]$**

The data from both RAS-LIF and RAS-MS experiments showed comprehensively that there was no significant change in the surface structure of $[C_{12}mim][BF_4]$ in passing from the SmA phase to the isotropic liquid. The RAS-LIF experiments revealed a weak, linear temperature dependence in the OH reactivity, which was continuous across the phase boundary. Additionally, no change in the OH rotational distribution was found within the resolution of the experiment. The RAS-MS data showed, *via* the angular and energy-transfer distributions, that between the SmA and isotropic phases the surface remained unaltered. Angular distributions are particularly sensitive to surface ordering and roughness[68, 69] and the absence of any change in these distributions is strong evidence of an unchanging surface. The surface energy transfer is sensitive to the local environment that the incident O-atoms strike and yields information about surface "softness" or "stiffness". Again, no change was found between the SmA and isotropic phases. Other metrics from the RAS-MS experiment confirmed this effect (Figures S6 and S7).

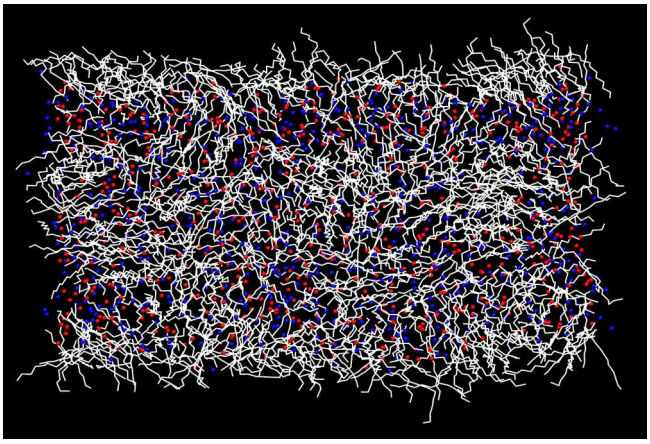

**Figure 7**. Side-view MD snapshot of $[C_{12}mim][BF_4]$ in the isotropic phase showing the $C_{12}$ cation chain (white lines), the center-of-mass of the cation imidazolium ring (blue spheres) and $BF_4^-$ (red spheres). The vacuum interface is at the top and bottom of the slab. Periodic boundary conditions exist at the left and right edges of the slab.

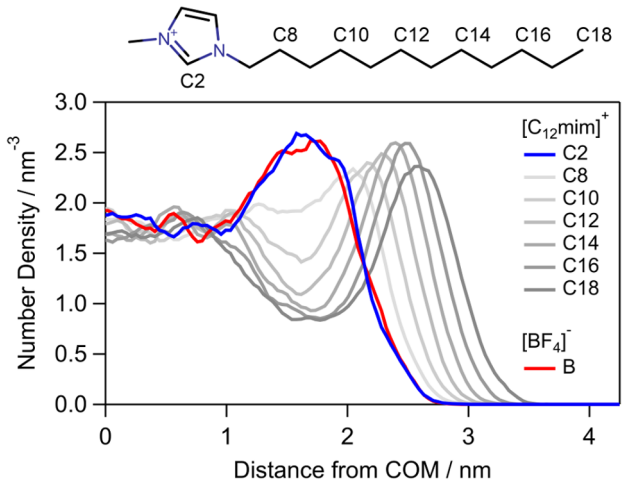


**Figure 8**. Atom density profiles along the surface normal for $[C_{12}mim][BF_4]$ in the isotropic phase, generated from MD simulations. Profiles are shown for selected positions in the molecular structure, as indicated. The center of the liquid slab was defined by its center-of-mass. Density profiles were averaged over both ionic liquid-vacuum interfaces and over a 1 ns interval.

It is not too naïve to expect that the surface structure would change for ILCs between phases given that for LCs, well into the isotropic phase, the surface can have a random structure determined by capillary waves, which then becomes smectic in character as a SmA transition is approached.[12] Therefore, it might at first sight be surprising that no apparent SmA-Iso transition is observed at the surface in this study. However, considering for a moment, only the isotropic phase of ILs, there is a general consensus[21, 22,38] about how the vacuum interface is ordered: namely that it consists of an alkyl-rich outer layer and an underlying sub-surface layer that is rich

in head groups and anions. This layering generally has the form of a damped density oscillation, tending toward the bulk value as the distance into the bulk and away from the surface is increased. For the specific case of the $[C_{12}mim][BF_4]$ liquid-vacuum-interface, molecular dynamics (MD) simulations were used to examine the surface structure in the isotropic phase; simulations of the more complex liquid crystal phase were not attempted. Details of the simulation are stated in the SI and in a previous publication.[51] The results from the simulations are shown in Figure 7, where an MD snapshot provides a qualitative picture of the surface structure, and in Figure 8, where atom density profiles along the liquid slab surface normal provide a quantitative description.

Figures 7 and 8 both show that the $[C_{12}mim][BF_4]$ surface also possesses the characteristic surface layering as described above with the $C_{12}$ chain on the cation projecting predominantly out toward the vacuum, while the charged head group and $BF_4^-$ anion form pairs in a sub-surface layer. Additionally, as confirmed widely in dedicated simulations of the isotropic bulk, it is also significantly ordered, with lamellar non-polar domains interpenetrated by polar regions, but it is notable that these are *not* oriented on average relative to the surface.[16]

Since no significant change was observed in either RAS-LIF or RAS-MS experiments on $[C_{12}mim][BF_4]$ as the temperature was lowered across the Iso to SmA phase boundary, this leads to the unambiguous conclusion that the outer surface structure of $[C_{12}mim][BF_4]$ in the SmA phase remains unchanged. The surface structure is presumably still driven by the dominant interaction between the cation-anion pairs, creating significant local organization at the outer surface, very similar to that shown in Figures 7 and 8. What is still unknown is how the structural and orientational order of the bulk SmA phase and surface-induced layering are mediated to allow these different structures to coexist. Presumably, some gradual decay or discrete

termination of the sub-surface layers occurs as observed in conventional liquid crystals.[11, 12] The penetration depth of the O-atom experiments in this study is such that only the outermost molecules are expected to be probed[70] and such sub-surface layering is unlikely to be detected. Other surface-specific methods would be better suited to exploring this sub-surface layering.[41] In summary, it seems that there is little if any correlation between the bulk and surface order for $[C_{12}mim][BF_4]$.

For the RAS-LIF experiment, the change in OH reactivity between 30.5 °C in the SmA phase and 65.0 °C in the isotropic phase was ~15%, and by measuring additional temperatures further into the isotropic region, a modest but repeatable linear increase in OH reactivity was found relative to either squalane or $[C_{12}mim][Tf_2N]$ over the same temperature range. The corresponding gradient was ~0.4% of OH reactivity per °C up to 109 ºC, the maximum liquid temperature measured. As mentioned above, the lack of change in the gradient of reactivity with temperature across the phase boundary of $[C_{12}mim][BF_4]$ suggests that the surface and bulk order are not related and that the modest, monotonic increase in reactivity relative to either squalane or $[C_{12}mim][Tf_2N]$, is driven by a process independent of the bulk order. This may be related to the $[C_{12}mim][BF_4]$ surface being more densely packed with alkyl chains[51] compared to that of $[C_{12}mim][Tf_2N]$, on account of the different size of the two anions. For $[C_{18}mim][FAP]$ (FAP = *mer-tris*(pentafluoroethyl)trifluorophosphate(V)), Mezger *et al*.[41] observed a linear contraction of the ionic layering as the temperature was increased in the isotropic phase. $[C_{18}mim][FAP]$ does not have a liquid crystal phase, and the decreased lamellar spacing was ascribed to the alkyl chains adopting *gauche* conformations, contracting the layers. At the same time, the alkyl chains spread out along the surface, increasing the density of surface-parallel area per chain. RAS-LIF is very sensitive to $CH_2$ unit density so only a modest rearrangement would be required to see an

increase in reactivity. For $[C_{12}mim][Tf_2N]$, which has a less alkyl-rich surface, it is possible that the alkyl chains are already spread out across the surface and that increasing the temperature results in a less significant change in surface structure.

An alternative proposal is that structural re-arrangement of the $[C_{12}mim][BF_4]$ surface may reduce the probability of the secondary reaction to form $H_2O$, which would effectively increase the reactivity. If this is true, there should have been a corresponding increase in the yield of $H_2O$ as the temperature was increased. RAS-LIF is not sensitive to $H_2O$, but results from RAS-MS (Figure S6) show effectively no change in the $O/H_2O$ product ratio with increasing temperature, contrary to the prediction. However, since the two experiments operate with very different collision energies, this comparison might not be definitive. Finally, as Figure 3b shows a linear relation with temperature and not an exponential increase, a thermal contribution to surmounting the activation barrier for H abstraction can be discounted reliably.

**8CB: Effect of bulk order on surface structure**

The comparative experiments on the well-known liquid crystal, 8CB, using the RAS-LIF method, were carried out primarily to help understand the results from $[C_{12}mim][BF_4]$. Unexpectedly, the 8CB data showed a very clear step change in the OH reactivity in moving from the SmA to the N phase, but no change between the N and Iso phases. One observation of note is that for the bulk material, the transition between the SmA and N phase is second order thermodynamically, yet the reactivities appear to show a first-order change. In reality, the temperature resolution of the experiment is probably insufficient to be able to describe the transition and so it is believed that the first-order appearance of the change may in fact simply represent points measured either side of the transition. Two questions arise from these data:

firstly, why is there is a single sharp change in the reactivity, and secondly, why does it occur at the SmA-N transition?

A mechanical effect due to the use of a scraper in the experiment was considered as a possible source of the change at the SmA-N transition because, in principle, this may have the ability to induce a planar alignment in the smectic phase. This could result in a different availability of alkyl chains at the surface. However, this argument ought to apply equally to $[C_{12}mim][BF_4]$ and should have led to a difference in signal intensity between its SmA and Iso phases, which is not observed. Furthermore, in some experiments the wheel rotation was stopped while the 8CB was in the SmA phase and no increase in signal was observed, which would have been expected if there was reorientation from a rotation-induced planar to a homeotropic alignment. With mechanical effects seeming unlikely to cause the step change, the shapes of the appearance profiles from the RAS-LIF experiments are now examined in more detail to see whether they contain further clues to the origin of this observation.

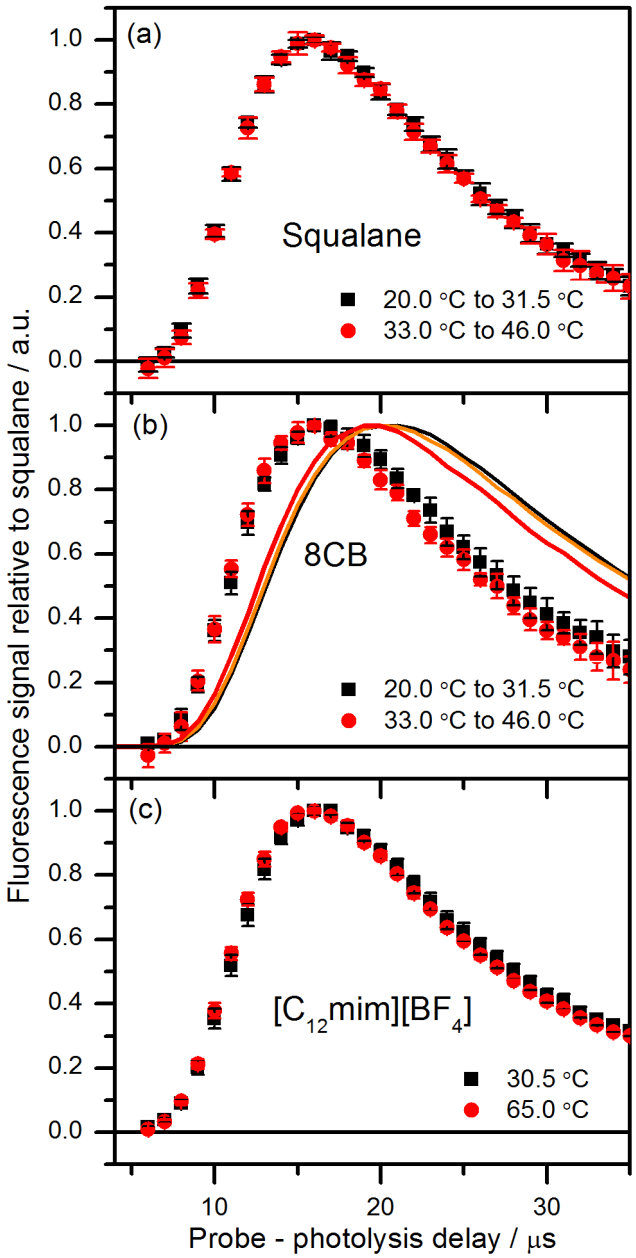


**Figure 9.** a) Normalized appearance profiles at different liquid temperatures for a) squalane, b) 8CB, and c) $[C_{12}mim][BF_4]$. Also shown in b) is a TD only simulation for surface temperatures 25 °C (black line), 39 °C (orange line), and 70 °C (red line). All error bars are 95% CL.

Figure 9a shows normalized appearance profiles from squalane when averaged over the respective temperature ranges corresponding to the SmA and nematic/isotropic phases, respectively, of 8CB. The temperatures can be termed "cold" and "hot" for convenience. For squalane, the cold and hot average temperature profiles overlap well, suggesting no significant change in the surface structure with temperature, as expected.[60] By comparison, Figure 9b shows the normalized appearance profiles for 8CB averaged over the same two temperature ranges. It can be seen that the cold profile differs systematically from the hot profile, particularly in the region beyond the peak. If the cold and hot profiles for 8CB are compared with the squalane profiles, the hot 8CB profile overlaps well with both squalane profiles. This leads to the conclusion that it is the cold 8CB profile that is anomalous by having a higher proportion of slower-moving OH. Figure 9c shows that for $[C_{12}mim][BF_4]$, the two selected discrete profiles at 30.5 °C and 65.0 °C overlap well, despite the larger temperature difference. This is additional evidence that the surface of this liquid remains unchanged with temperature, again in contrast to 8CB.

The possibility was considered that the differences between the cold and hot profiles for 8CB result from a purely thermal effect on the speeds of a thermalized component of the products. However, this can be discounted because, as Figure 9b shows, the effect on a simulated TD distribution[60] of a temperature change from 25 °C to 39 °C (the average temperatures of the respective low and high-temperature profiles), is much smaller than the empirical difference between the 8CB profiles. An unphysically large surface temperature difference of 70 °C is required to reproduce the observed difference in profiles. Furthermore, it is not clear why such a purely thermal effect would affect 8CB and not equally $[C_{12}mim][BF_4]$ or squalane.

It is also not obvious that the results for 8CB are a straightforward effect of thermal roughening. It is generally understood that the IS/TD ratio decreases with temperature owing to the increased thermal fluctuations of the surface, which enhance trapping desorption type interactions.[47] This is the opposite of the apparent change in the balance of IS and TD components in the observed 8CB profiles, if the slower moving tail is associated with a TD component. Therefore, it seems likely that the increased density of slower moving OH in the cold normalized 8CB appearance profile is due to a specific change in surface structure that acts in the opposite sense to normal thermal roughening.

Simulations have shown that the air-liquid interface induces smectic layering in the nematic and isotropic phases for the related material 5CB (which does not have an underlying SmA phase).[71] If this is also true for 8CB, then changes in the bulk order must influence the surface-induced layering in some way that is present on both sides of the SmA-to-N phase transition. This leads to the possible conclusion that the SmA surface may be rougher, or more corrugated, compared to the nematic and isotropic surfaces. This roughness could conceivably occur on length scales corresponding to multiple molecules clustered in domains, while on the molecular length scale, the antiparallel arrangement of the 8CB molecules at the surface is maintained.[30] Due to this roughness, the nascent OH would have more chance of sustaining multiple collisions, not only increasing the amount of slower-moving OH but also reducing the overall yield of OH from the SmA surface. This could either be directly because of lower accessibility of the reactive secondary $CH_2$ units in the octyl chain, or indirectly through a lower escape probability of the nascent OH and a corresponding higher probability of forming the secondary product $H_2O$ (unobserved in RAS-LIF). It may be conceptually reasonable that the more fluid nematic and isotropic phases allow a greater degree of relaxation of the surface-induced layers, reducing the

overall degree of corrugation. This is an interesting, reasonable, but perhaps tentative, hypothesis that clearly remains to be verified, either through comparative measurements of OH yields from a wider range of liquid crystals or using independent, complementary techniques sensitive to surface structure.

## Conclusion

The surfaces of $[C_{12}mim][BF_4]$ in the SmA and Iso phases were studied using reactive atom scattering. A weak linear temperature dependence in OH reactivity was revealed by RAS-LIF; however, this dependence was unperturbed at the transition from the SmA to the Iso phase. This effect was attributed to a thermally induced gradual re-ordering of the surface as opposed to any sharp change accompanying the change in bulk order.

A more detailed study of $[C_{12}mim][BF_4]$ using RAS-MS revealed that there was no change in the angular distributions of the scattered species between the SmA and Iso phases, indicating that the surface roughness was essentially unchanged between phases. Similar results were found for the surface energy transfer and other metrics (product ratios and IS/TD ratio).

As the RAS-LIF and RAS-MS methods are only sensitive to the outermost molecules of the liquid surface, this leads to the conclusion that the outer-most layer of the $[C_{12}mim][BF_4]$ surface is unchanged between the SmA and Iso phases, despite the large change in bulk order. This suggests strongly that the dominance of the outer surface by alkyl chains above an underlying layer rich in anions and cation head groups, well known for the isotropic phases of related ionic liquids, also persists in the SmA phase.

In comparative measurements, the surface of 8CB was studied using RAS-LIF. A significant and sharp increase in OH reactivity was found at the transition between the SmA and the N/Iso phases. It is suggested tentatively that this change in OH reactivity may be due to the bulk order

of the SmA phase making the surface more corrugated, either hindering access to the reactive sites in the octyl chain or facilitating secondary loss of nascent OH to form water.

## Author Information

Corresponding authors: *Email: tminton@montana.edu and K.G.McKendrick@hw.ac.uk

## Acknowledgements

The authors acknowledge helpful discussions from Professor Robert Richardson at University of Bristol, United Kingdom. This work was funded jointly by the U.K. Engineering and Physical Sciences Research Council (EP/K032062/1) and the U.S. National Science Foundation (NSF-CHE-1266032).

## Supporting Information

Description of synthesis of $[C_{12}mim][Tf_2N]$. RAS-LIF and RAS-MS experimental details. RAS-MS TOF analysis. Rotational OH LIF excitation spectra details and population graphs for $[C_{12}mim][BF_4]$ and 8CB. Analysis of HONO contribution to 8CB reactivities. RAS-MS O/OH and $O/H_2O$ product ratios. IS/TD ratios for O, OH, and $H_2O$. Additional information on MD simulations.

## References

1. Jerome, B. Surface Effects and Anchoring in Liquid Crystals. *Rep. Prog. Phys.* **1991,** *54* (3), 391.
2. Lovelock, K. R. J. Influence of the Ionic Liquid/Gas Surface on Ionic Liquid Chemistry. *Phys. Chem. Chem. Phys.* **2012,** *14* (15), 5071-5089.
3. Plechkova, N. V.; Seddon, K. R. Applications of Ionic Liquids in the Chemical Industry. *Chem. Soc. Rev.* **2008,** *37* (1), 123-150.
4. Krossing, I.; Slattery, J. M.; Daguenet, C.; Dyson, P. J.; Oleinikova, A.; Weingärtner, H. Why Are Ionic Liquids Liquid? A Simple Explanation Based on Lattice and Solvation Energies. *J. Am. Chem. Soc.* **2006,** *128* (41), 13427-13434.

5. Preiss, U. P. R. M.; Slattery, J. M.; Krossing, I. In Silico Prediction of Molecular Volumes, Heat Capacities, and Temperature-Dependent Densities of Ionic Liquids. *Ind. Eng. Chem. Res.* **2009,** *48* (4), 2290-2296.
6. Binnemans, K. Ionic Liquid Crystals. *Chem. Rev.* **2005,** *105* (11), 4148-4204.
7. Goossens, K.; Lava, K.; Bielawski, C. W.; Binnemans, K. Ionic Liquid Crystals: Versatile Materials. *Chem. Rev.* **2016,** *116* (8), 4643-4807.
8. Shibaev, P. V.; Wenzlick, M.; Murray, J.; Tantillo, A.; Howard-Jennings, J. Rebirth of Liquid Crystals for Sensoric Applications: Environmental and Gas Sensors. *Adv. Condens. Matter Phys.* **2015,** *2015*, 8.
9. Hoogboom, J.; Rasing, T.; Rowan, A. E.; Nolte, R. J. M. LCD Alignment Layers. Controlling Nematic Domain Properties. *J. Mater. Chem.* **2006,** *16* (14), 1305-1314.
10. Pershan, P. S.; Braslau, A.; Weiss, A. H.; Als-Nielsen, J. Smectic Layering at the Free Surface of Liquid Crystals in the Nematic Phase: X-Ray Reflectivity. *Phys. Rev. A* **1987,** *35* (11), 4800-4813.
11. Lau, Y. G. J.; Richardson, R. M.; Dalgliesh, R. M.; Zimmermann, H. Surface Ordering at the Air–Nematic Interface. Part 1. A Neutron Reflection Study of Translational Order. *Liq. Cryst.* **2007,** *34* (3), 333-341.
12. Ocko, B. M.; Braslau, A.; Pershan, P. S.; Als-Nielsen, J.; Deutsch, M. Quantized Layer Growth at Liquid-Crystal Surfaces. *Phys. Rev. Lett.* **1986,** *57* (1), 94-97.
13. Lucht, R.; Marczuk, P.; Bahr, C.; Findenegg, G. H. X-Ray Reflectivity Study of Smectic Wetting and Prewetting at the Free Surface of Isotropic Liquid Crystals. *Phys. Rev. E* **2001,** *63* (4), 041704.
14. Triolo, A.; Russina, O.; Bleif, H.-J.; Di Cola, E. Nanoscale Segregation in Room Temperature Ionic Liquids. *J. Phys. Chem. B* **2007,** *111* (18), 4641-4644.
15. Shimizu, K.; Bernardes, C. E. S.; Canongia Lopes, J. N. Structure and Aggregation in the 1-Alkyl-3-Methylimidazolium Bis(trifluoromethylsulfonyl)imide Ionic Liquid Homologous Series. *J. Phys. Chem. B* **2014,** *118* (2), 567-576.
16. Hayes, R.; Warr, G. G.; Atkin, R. Structure and Nanostructure in Ionic Liquids. *Chem. Rev.* **2015,** *115* (13), 6357-6426.
17. Castner, E. W.; Margulis, C. J.; Maroncelli, M.; Wishart, J. F. Ionic Liquids: Structure and Photochemical Reactions. *Annu. Rev. Phys. Chem.* **2011,** *62* (1), 85-105.
18. Sloutskin, E.; Ocko, B. M.; Tamam, L.; Kuzmenko, I.; Gog, T.; Deutsch, M. Surface Layering in Ionic Liquids: An X-ray Reflectivity Study. *J. Am. Chem. Soc.* **2005,** *127* (21), 7796-7804.
19. Bowers, J.; Vergara-Gutierrez, M. C.; Webster, J. R. P. Surface Ordering of Amphiphilic Ionic Liquids. *Langmuir* **2004,** *20* (2), 309-312.
20. Nishi, N.; Uruga, T.; Tanida, H.; Kakiuchi, T. Temperature Dependence of Multilayering at the Free Surface of Ionic Liquids Probed by X-ray Reflectivity Measurements. *Langmuir* **2011,** *27* (12), 7531-7536.
21. Lynden-Bell, R. M.; Del Popolo, M. Simulation of the Surface Structure of Butylmethylimidazolium Ionic Liquids. *Phys. Chem. Chem. Phys.* **2006,** *8* (8), 949-954.
22. Li, X.; Schatz, G. C.; Nesbitt, D. J. Anion Effects in the Scattering of $CO_2$ from the Room-Temperature Ionic Liquids [bmim][$BF_4$] and [bmim][$Tf_2N$]: Insights from Quantum Mechanics/Molecular Mechanics Trajectories. *J. Phys. Chem. B* **2012,** *116* (11), 3587-3602.

23. Jiang, W.; Wang, Y.; Yan, T.; Voth, G. A. A Multiscale Coarse-Graining Study of the Liquid/Vacuum Interface of Room-Temperature Ionic Liquids with Alkyl Substituents of Different Lengths. *J. Phys. Chem. C* **2008,** *112* (4), 1132-1139.
24. Fukuhara, K.; Nagano, S.; Hara, M.; Seki, T. Free-Surface Molecular Command Systems for Photoalignment of Liquid Crystalline Materials. *Nat. Commun.* **2014,** *5*, 3320.
25. Wang, X.; Sobota, M.; Kohler, F. T. U.; Morain, B.; Melcher, B. U.; Laurin, M.; Wasserscheid, P.; Libuda, J.; Meyer, K. Functional Nickel Complexes of N-Heterocyclic Carbene Ligands in Pre-Organized and Supported Thin Film Materials. *J. Mater. Chem.* **2012,** *22* (5), 1893-1898.
26. Carmichael, A. J.; Hardacre, C.; Holbrey, J. D.; Nieuwenhuyzen, M.; Seddon, K. R. Molecular Layering and Local Order in Thin Films of 1-Alkyl-3-Methylimidazolium Ionic Liquids Using X-Ray Reflectivity. *Mol. Phys.* **2001,** *99* (10), 795-800.
27. McIntosh, E. M.; Ellis, J.; Jardine, A. P.; Licence, P.; Jones, R. G.; Allison, W. Probing Liquid Behaviour by Helium Atom Scattering: Surface Structure and Phase Transitions of an Ionic Liquid on Au(111). *Chem. Sci.* **2014,** *5* (2), 667-676.
28. D. Holbrey, J.; R. Seddon, K. The Phase Behaviour of 1-Alkyl-3-Methylimidazolium Tetrafluoroborates; Ionic Liquids and Ionic Liquid Crystals. *J. Chem. Soc., Dalton Trans.* **1999,** (13), 2133-2140.
29. Biensan, C.; Desbat, B.; Turlet, J. M. Molecular Orientation of a Cyanobiphenyl Liquid Crystal in Freely Suspended Films and at the Air-Water Interface. *Thin Solid Films* **1996,** *284–285*, 293-296.
30. Guyot-Sionnest, P.; Hsiung, H.; Shen, Y. R. Surface Polar Ordering in a Liquid Crystal Observed by Optical Second-Harmonic Generation. *Phys. Rev. Lett.* **1986,** *57* (23), 2963-2966.
31. Palermo, M. F.; Muccioli, L.; Zannoni, C. Molecular Organization in Freely Suspended Nano-Thick 8CB Smectic films. An Atomistic Simulation. *Phys. Chem. Chem. Phys.* **2015,** *17* (39), 26149-26159.
32. Wakeham, D.; Nelson, A.; Warr, G. G.; Atkin, R. Probing the Protic Ionic Liquid Surface Using X-Ray Reflectivity. *Phys. Chem. Chem. Phys.* **2011,** *13* (46), 20828-20835.
33. Nishi, N.; Kasuya, K.; Kakiuchi, T. Surface Structure of a Hydrophobic Ionic Liquid Probed by Spectroscopic Ellipsometry. *J. Phys. Chem. C* **2012,** *116* (8), 5097-5102.
34. Beattie, D. A.; Harmer-Bassell, S. L.; Ho, T. T. M.; Krasowska, M.; Ralston, J.; Sellapperumage, P. M. F.; Wasik, P. Spectroscopic Study of Ionic Liquid Adsorption from Solution onto Gold. *Physical Chemistry Chemical Physics* **2015,** *17* (6), 4199-4209.
35. Villar-Garcia, I. J.; Fearn, S.; Ismail, N. L.; McIntosh, A. J. S.; Lovelock, K. R. J. Fine Tuning the Ionic Liquid-Vacuum Outer Atomic Surface using Ion Mixtures. *Chem. Commun.* **2015,** *51* (25), 5367-5370.
36. Gannon, T. J.; Law, G.; Watson, P. R.; Carmichael, A. J.; Seddon, K. R. First Observation of Molecular Composition and Orientation at the Surface of a Room-Temperature Ionic Liquid. *Langmuir* **1999,** *15* (24), 8429-8434.
37. Kauling, A.; Ebeling, G.; Morais, J.; Pádua, A.; Grehl, T.; Brongersma, H. H.; Dupont, J. Surface Composition/Organization of Ionic Liquids with Au Nanoparticles Revealed by High-Sensitivity Low-Energy Ion Scattering. *Langmuir* **2013,** *29* (46), 14301-14306.
38. Steinruck, H.-P. Recent Developments in the Study of Ionic Liquid Interfaces Using X-Ray Photoelectron Spectroscopy and Potential Future Directions. *Phys. Chem. Chem. Phys.* **2012,** *14* (15), 5010-5029.

39. Jr., E. W. C.; Margulis, C. J.; Maroncelli, M.; Wishart, J. F. Ionic Liquids: Structure and Photochemical Reactions. *Annu. Rev. Phys. Chem.* **2011,** *62* (1), 85-105.
40. Caporali, S.; Bardi, U.; Lavacchi, A. X-ray photoelectron spectroscopy and low energy ion scattering studies on 1-buthyl-3-methyl-imidazolium bis(trifluoromethane) sulfonimide. *Journal of Electron Spectroscopy and Related Phenomena* **2006,** *151* (1), 4-8.
41. Mezger, M.; Ocko, B. M.; Reichert, H.; Deutsch, M. Surface Layering and Melting in an Ionic Liquid Studied by Resonant Soft X-Ray Reflectivity. *Proc. Nat. Acad. Sci. U.S.A.* **2013,** *110* (10), 3733-3737.
42. Penalber, C. Y.; Grenoble, Z.; Baker, G. A.; Baldelli, S. Surface Characterization of Imidazolium-Based Ionic Liquids with Cyano-Functionalized Anions at the Gas-Liquid Interface using Sum Frequency Generation Spectroscopy. *Phys. Chem. Chem. Phys.* **2012,** *14* (15), 5122-5131.
43. Saha, A.; SenGupta, S.; Kumar, A.; Choudhury, S.; Naik, P. D. Vibrational Sum–Frequency Generation Spectroscopy of Ionic Liquid 1-Butyl-3-Methylimidazolium tris(pentafluoroethyl)trifluorophosphate at the Air–Water Interface. *Chem. Phys.* **2016,** *475*, 14-22.
44. Yockel, S.; Schatz, G. C. Modeling O($^3$P) and Ar Scattering from the Ionic Liquid [emim][$NO_3$] at 5 eV with Hybrid QM/MM Molecular Dynamics. *J. Phys. Chem. B* **2010,** *114* (45), 14241-14248.
45. Zutz, A.; Nesbitt, D. J. Nonadiabatic Spin–Orbit Excitation Dynamics in Quantum-State-Resolved NO($^2\Pi_{1/2}$) Scattering at the Gas–Room Temperature Ionic Liquid Interface. *J. Phys. Chem. C* **2015,** *119* (16), 8596-8607.
46. Janda, K. C.; Hurst, J. E.; Becker, C. A.; Cowin, J. P.; Auerbach, D. J.; Wharton, L. Direct Measurement of Velocity Distributions in Argon Beam–Tungsten Surface Scattering. *J. Chem. Phys.* **1980,** *72* (4), 2403-2410.
47. King, M. E.; Saecker, M. E.; Nathanson, G. M. The Thermal Roughening of Liquid Surfaces and its Effect on Gas–Liquid Collisions. *J. Chem. Phys.* **1994,** *101* (3), 2539.
48. Zolot, A. M.; Dagdigian, P. J.; Nesbitt, D. J. Quantum-State Resolved Reactive Scattering at the Gas-Liquid Interface: F+squalane ($C_{30}H_{62}$) Dynamics *via* High-Resolution Infrared Absorption of Nascent HF($v$,$J$). *J. Chem. Phys.* **2008,** *129* (19), 194705.
49. Kelso, H.; Köhler, S. P. K.; Henderson, D. A.; McKendrick, K. G. Dynamics of the Gas–Liquid Interfacial Reaction of O($^3$P) Atoms with Hydrocarbons. *J. Chem. Phys.* **2003,** *119* (19), 9985-9988.
50. Zhang, J.; Garton, D. J.; Minton, T. K. Reactive and Inelastic Scattering Dynamics of Hyperthermal Oxygen Atoms on a Saturated Hydrocarbon Surface. *J. Chem. Phys.* **2002,** *117* (13), 6239.
51. Tesa-Serrate, M. A.; Marshall, B. C.; Smoll, E. J.; Purcell, S. M.; Costen, M. L.; Slattery, J. M.; Minton, T. K.; McKendrick, K. G. Ionic Liquid–Vacuum Interfaces Probed by Reactive Atom Scattering: Influence of Alkyl Chain Length and Anion Volume. *J. Phys. Chem. C* **2015,** *119* (10), 5491-5505.
52. Waring, C.; Bagot, P. A. J.; Slattery, J. M.; Costen, M. L.; McKendrick, K. G. O($^3$P) Atoms as a Chemical Probe of Surface Ordering in Ionic Liquids. *J. Phys. Chem. A* **2010,** *114* (14), 4896-4904.
53. Troya, D. Barriers of Hydrogen Abstraction from Primary, Secondary, and Tertiary Alkane Sites by O($^3$P). *J. Phys. Chem. A* **2007,** *111* (42), 10745-10753.

54. Wu, B.; Zhang, J.; Minton, T. K.; McKendrick, K. G.; Slattery, J. M.; Yockel, S.; Schatz, G. C. Scattering Dynamics of Hyperthermal Oxygen Atoms on Ionic Liquid Surfaces: [emim][$NTf_2$] and [$C_{12}$mim][$NTf_2$]. *J. Phys. Chem. C* **2010,** *114* (9), 4015-4027.
55. Alexander, W. A.; Zhang, J.; Murray, V. J.; Nathanson, G. M.; Minton, T. K. Kinematics and Dynamics of Atomic-Beam Scattering on Liquid and Self-Assembled Monolayer Surfaces. *Faraday Discuss.* **2012,** *157* (0), 355-374.
56. Bier, M.; Dietrich, S. Vapour Pressure of Ionic Liquids. *Mol. Phys.* **2010,** *108* (2), 211-214.
57. Poole, P. L.; Andereck, C. D.; Schumacher, D. W.; Daskalova, R. L.; Feister, S.; George, K. M.; Willis, C.; Akli, K. U.; Chowdhury, E. A. Liquid Crystal Films as On-Demand, Variable Thickness (50–5000 nm) Targets for Intense Lasers. *Phys. Plasmas* **2014,** *21* (6), 063109.
58. Faust, J. A.; Nathanson, G. M. Microjets and Coated Wheels: Versatile Tools for Exploring Collisions and Reactions at Gas-Liquid Interfaces *Chem. Soc. Rev.* [Online], **2016**. DOI: 10.1039/C6CS00079G. http://dx.doi.org/10.1039/C6CS00079G.
59. Baker, R. P.; Costen, M. L.; Hancock, G.; Ritchie, G. A. D.; Summerfield, D. Vector Correlations in the 355 nm Photolysis of Thermal $NO_2$. *Phys. Chem. Chem. Phys.* **2000,** *2* (4), 661-664.
60. Allan, M.; Bagot, P. A. J.; Costen, M. L.; McKendrick, K. G. Temperature Dependence of OH Yield, Translational Energy, and Vibrational Branching in the Reaction of $O(^3P)$(g) with Liquid Squalane. *J. Phys. Chem. C* **2007,** *111* (40), 14833-14842.
61. Barry, N. J.; Fletcher, I. W.; Whitehead, J. C. The Dynamics of OH Production in the Reaction Atomic $O(^3P)$ + Benzene. *J. Phys. Chem.* **1986,** *90* (21), 4911-4912.
62. Garton, D. J.; Brunsvold, A. L.; Minton, T. K.; Troya, D.; Maiti, B.; Schatz, G. C. Experimental and Theoretical Investigations of the Inelastic and Reactive Scattering Dynamics of $O(^3P)$ + $D_2$. *J. Phys. Chem. A* **2006,** *110* (4), 1327-1341.
63. Garton, D. J.; Minton, T. K.; Maiti, B.; Troya, D.; Schatz, G. C. A Crossed Molecular Beams Study of the $O(^3P)$+$H_2$ Reaction: Comparison of Excitation Function with Accurate Quantum Reactive Scattering Calculations. *J. Chem. Phys.* **2003,** *118* (4), 1585-1588.
64. Brink, G. O. Electron Bombardment Molecular Beam Detector. *Rev. Sci. Instrum.* **1966,** *37* (7), 857-860.
65. Daly, N. R. Scintillation Type Mass Spectrometer Ion Detector. *Rev. Sci. Instrum.* **1960,** *31* (3), 264.
66. Luque, J.; Crosley, D. R. *LIFBASE: Database and spectral simulation (version 1.5)*, SRI International Report MP 99-009: 1999.
67. Saecker, M. E.; Govoni, S. T.; Kowalski, D. V.; King, M. E.; Nathanson, G. M. Molecular Beam Scattering from Liquid Surfaces. *Science* **1991,** *252* (5011), 1421-1424.
68. Marshall, B. C.; Smoll, E. J.; Purcell, S. M.; Costen, M. L.; McKendrick, K. G.; Minton, T. K. Scattering Dynamics of Oxygen Atoms on Imidazolium Tetrafluoroborate Ionic Liquid Surfaces: Dependence on Alkyl Chain Length. *J. Phys. Chem. C* **2016,** *120* (23), 12472-12483.
69. King, M. E.; Fiehrer, K. M.; Nathanson, G. M.; Minton, T. K. Effects of Thermal Roughening on the Angular Distributions of Trapping and Scattering in Gas–Liquid Collisions. *J. Phys. Chem. A* **1997,** *101* (36), 6556-6561.
70. Waring, C.; Bagot, P. A. J.; Räisänen, M. T.; Costen, M. L.; McKendrick, K. G. Dynamics of the Reaction of $O(^3P)$ Atoms with Alkylthiol Self-assembled Monolayers. *J. Phys. Chem. A* **2009,** *113* (16), 4320-4329.

71. Pizzirusso, A.; Berardi, R.; Muccioli, L.; Ricci, M.; Zannoni, C. Predicting surface anchoring: molecular organization across a thin film of 5CB liquid crystal on silicon. *Chem. Sci.* **2012,** *3* (2), 573-579.

## TOC Graphic